Langmuir, 2019, published 08/06/2019; DOI: 10.1021/acs.langmuir.9b01375

In-situ small-angle neutron scattering investigation of adsorption-induced deformation in silica with hierarchical porosity

Lukas Ludescher[1,#], Roland Morak[1,#], Christian Balzer[2], Anna M. Waag[2], Stephan Braxmeier[2], Florian Putz[3], Sebastian Busch[4], Gennady Y. Gor[5], Alexander V. Neimark[6], Nicola Hüsing[3], Gudrun Reichenauer[2], Oskar Paris[1,*]

[1] *Institute of Physics, Montanuniversitaet Leoben, Franz-Josef-Str. 18, 8700 Leoben, Austria*
[2] *Bavarian Center for Applied Energy Research, Magdalene-Schoch-Str. 3, 97074 Wuerzburg, Germany*
[3] *Paris Lodron University Salzburg, Department of Chemistry and Physics of Materials, Jakob-Haringer Str. 2A, 5020 Salzburg, Austria*
[4] *German Engineering Materials Science Centre (GEMS) at Heinz Maier-Leibnitz Zentrum (MLZ), Helmholtz-Zentrum Geesthacht GmbH, Lichtenbergstrasse 1, Garching bei München, 85747, Germany*
[5] *Otto H. York Department of Chemical, and Materials Engineering, New Jersey Institute of Technology, University Heights, Newark, New Jersey 07102, United States*
[6] *Department of Chemical and Biochemical Engineering, Rutgers, The State University of New Jersey, 98 Brett Road, Piscataway, New Jersey 08854, United States*

# These two authors contributed equally to the work

* Corresponding author: oskar.paris@unileoben.ac.at

Keywords: Adsorption-induced deformation, ordered mesoporous silica, water adsorption, small-angle neutron scattering.

Abstract

The water adsorption-induced deformation of a series of silica samples with hierarchical porosity has been studied by in-situ small-angle neutron scattering (SANS) and in-situ dilatometry. The monolithic samples consisted of a disordered macroporous network of struts formed by a 2D lattice of hexagonally-ordered cylindrical mesopores, and disordered micropores within the mesopore walls. Strain isotherms were obtained at the mesopore level by analyzing the shift of the Bragg reflections from the ordered mesopore lattice in the SANS data. Thus, SANS essentially measured the radial strain of the cylindrical mesopores including the volume changes of the mesopore walls due to micropore deformation. A H_2O/D_2O mixture with net zero coherent neutron scattering length density was employed in order to avoid apparent strain effects due to intensity changes during pore filling. In contrast to SANS, the strain isotherms obtained from in-situ dilatometry result from a combination of axial and radial mesopore deformation together with micropore deformation. SANS- and dilatometry strain data were quantitatively analyzed with a theoretical model for micro-/mesopore deformation by combining information from nitrogen and water adsorption isotherms to estimate the water-silica interaction. It was shown that in-situ SANS provides complementary information to dilatometry and allows a quantitative estimate of the elastic properties of the mesopore walls from water adsorption.

1. Introduction

Adsorption-induced deformation describes the effect that nanoporous materials tend to mechanically deform upon the adsorption of a fluid [1]. This might have implications for the mechanical integrity of the materials, in particular for highly porous materials such as aerogels [2-3] or compliant polymers [4], and possible applications of this effect for actuators have been proposed [5-7]. In mesoporous materials, this effect is determined by the interplay of expansive disjoining pressure due to solid-liquid interfacial energy changes (often called "Bangham effect") [8], and compressive capillary pressure due to curved liquid-gas interfaces. Capillary condensation in mesoporous materials separates the sample strain measured as a function of relative gas pressure p/p_0 (i.e., the "strain isotherm") typically into two regimes, a film regime and a filled pore regime with a discontinuous behavior at the transition and a hysteresis between adsorption and desorption. For a completely liquid-filled pore space at a relative gas pressure of $p/p_0 = 1$, a net expansion with respect to the empty reference state at $p/p_0 = 0$ is typically observed [3, 9-15]. Also microporous materials usually exhibit a net expansion at high relative pressures, while they may show a compression at low relative pressures due to packing effects [16-18].

The explicit calculation of the stresses and corresponding strains as a function of p/p_0 requires the combination of the thermodynamics of the system represented by the adsorption isotherm, and solid mechanics depending on the pore geometry and the mechanical properties of the pore walls. While many theoretical and/or computational studies treat the detailed adsorbate-adsorbent interactions [19], and numerous works have been published on the deformation of the pore space as a result of internal and external pressures (poromechanics) [20], the combined treatment of both aspects is more recent [21-32]. We have lately developed a general theoretical

framework to describe the adsorption- and the strain isotherms for cylindrical mesopores by combining the Derjaguin−Broekhoff−de Boer (DBdB) theory [33-35], the adsorption stress model [17], and the mechanical model of a cylindrical tube [14]. The model delivered analytical equations for the axial and radial adsorption stresses and corresponding strains, and allowed the quantitative comparison of the calculated strains during adsorption of nitrogen at 77 K with experimental strain isotherms [36]. The sample consisted of a macroporous network of interconnected struts, with each strut containing well-ordered and essentially monodisperse cylindrical mesopores. The experimental strain isotherm was determined from the macroscopic length change of the monolithic sample measured by in-situ dilatometry [3]. Since this macroscopic strain isotherm is determined by both, the axial and the radial stresses in the mesopores, a linear combination of these two components was used to model the data. In a successive paper, this theory was applied to a series of samples with similar macro- and mesopores, but exhibiting varying amounts of micropores within the mesopore walls [37]. By extending the theoretical model to include also micropore deformation, it was possible to satisfactorily describe the macroscopic strain isotherms, and to determine mechanical properties of the materials at the level of the mesopore walls, which are difficult to access by other methods.

In order to validate and complement these results, it is important to experimentally determine adsorption-induced deformation not only at the macroscopic but also directly at the mesopore level for two reasons: Firstly, the macroscopic strain contains both, the axial and radial strain contributions which cannot be separated unambiguously. Secondly, the macroscopic network can be expected to influence the mechanical response of the system to some extent. The axial deformation of cylindrical mesopores is only in very few cases directly accessible, namely when

these pores are macroscopically aligned, e.g. in thin films with the cylinder axis perpendicular to the surface [14-15]. In contrast, the radial strain from a hexagonally ordered array of cylindrical pores (typical systems being MCM-41 [38] or SBA-15 [39]) can in principle be determined using in-situ small-angle X-ray scattering (SAXS) also for powder samples by simply measuring the relative shift of the Debye-Scherrer rings from the mesopore lattice as a function of relative gas pressure [13]. It was previously shown that from the filled pore regime of such SAXS strain isotherms, an elastic "pore load modulus" can be deduced and related to the mechanical properties of the pore walls [13-14, 40-41]. The adsorption stress model was found to quantitatively describe the SAXS strain isotherm for pentane adsorption in an MCM-41 sample, but for a SBA-15 sample only qualitative agreement with the model was obtained [42]. In a recent combined in-situ dilatometry and in-situ SAXS experiment, strain isotherms were obtained from the same silica monoliths [43]. They showed considerable differences particularly for the maximum strains close to $p/p_0 = 1$, which are however predicted by the theoretical model to be identical [36]. The reason for these discrepancies is that during film formation and capillary condensation in the pores, a three-phase system forms (pore walls, empty pore space, and liquid-like condensate) which introduces strong intensity changes in the SAXS signal [44]. Since the adsorption induced strains are very small (typically much smaller than 1%), this induces artefacts in the determination of the pore lattice strain [45], depending strongly on the electron density difference between the liquid and the solid pore walls, and in a subtle manner also on porosity and pore size distribution [46]. This problem can be overcome by employing small-angle neutron scattering (SANS) in conjunction with a zero scattering length density (Z-SLD) adsorbate. This approach was first demonstrated for the investigation of adsorption induced deformation for Z-SLD n-pentane in a sintered silica aerogel [47], and later on for CO_2 adsorption on disordered microporous

carbons [48]. Recently, we have for the first time applied in-situ SANS using Z-SLD water in conjunction with in situ dilatometry for the investigation of hierarchically porous silica [49].

Here we investigate in detail the strain isotherms of three hierarchically porous silica samples from an in-situ SANS experiment using a Z-SLD water mixture of 91.95 % H_2O and 8.05 % D_2O as an adsorbate. Two macro-/meso-/microporous samples with different amounts of micropores, and one macro-/mesoporous sample decorated with organic residues in the mesopore walls were investigated. We compare the SANS strain isotherms with macroscopic dilatometry strain isotherms from the same samples. Moreover, we use the N_2 adsorption isotherms in conjunction with the water adsorption isotherms to estimate the water-silica interaction, and apply the theoretical model from refs [36-37] to quantitatively describe both, the adsorption and the strain isotherms.

2. Materials and Methods

2.1 Model Materials

The synthesis protocol of the hierarchical structured porous silica was introduced by Brandhuber et al.[50] and is only described very briefly here: wet gels were generated by mixing tetrakis(2-hydroxyethyl)orthosilicate with an aqueous solution of Pluronic P123 in 1 M HCl in a weight ratio of Si/P123/HCl = 8.4/30/70. The homogenized sol was poured into cylindrical moulds with a radius of 5 mm. Subsequently, the solution was submitted to further aging at 313 K for 7 days. The received wet gels were demoulded, washed in ethanol (5 times within 3 days) and dried with supercritical CO_2 (T_c = 304.18 K; P_c = 7.38 MPa).

The synthesis results in opaque cylindrical monoliths, which exhibit hierarchical porosity consisting of a disordered network of macropores and hexagonally ordered cylindrical

mesopores (see **Fig. 1** and refs [36-37, 43, 51]). From the monolithic samples, thin disks were cut by a diamond saw.

The disk-like samples obtained from the above described synthesis are not pure silica but likely contain a significant amount of organic residues within the mesopore walls and on the mesopore surface like the structurally similar SBA-15 [50]. To prepare samples without organic residues, some disks were subjected to a calcination step at 500 °C for 3 h at ambient atmosphere. This post treatment removes the organic residues and introduces microporosity into the sample [37, 52]. To obtain samples exhibiting no organic residues and reduced microporosity, some of the already calcined sample material was sintered at 750 °C for 15 min at ambient atmosphere. Hence, we obtain three samples with distinctive thermal histories, which are denoted in the following as *as prepared*, *calcined* and *sintered* samples.

To prevent irreversible changes of the porous silica structure upon water adsorption, the *as prepared* and *calcined* samples were aged at 74 % relative humidity and 50 °C for 3 weeks. The *sintered* sample was subjected to repeated water adsorption cycles until the adsorption isotherms became reproducible. Eventually, all samples were conditioned for 2 days in a mixture of 91.95 wt% water (H_2O) and 8.05 wt% heavy water (D_2O) at ambient temperature. As a consequence, all solvent-accessible exchangeable H-groups in the samples were adapted to the H/D ratio of the Z-SLD water used as adsorbate in the in-situ SANS experiments.

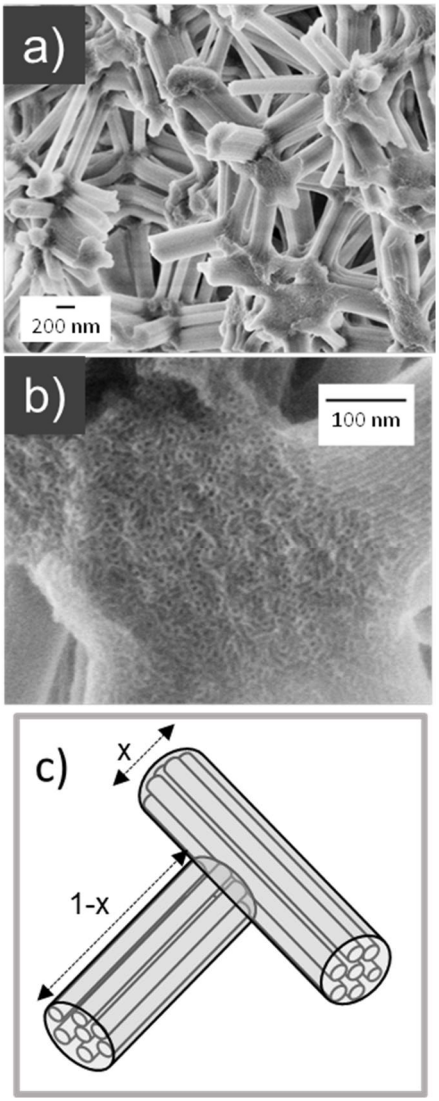

Figure 1: *Scanning electron microscopy (SEM) images of the as prepared sample showing the macroporous strut network (a), and the ordered mesopore arrangement inside the struts (b). c) shows a sketch of two struts and with the parameter x being the relative contributions of the axial and the radial strains, respectively to the macroscopic strain.*

2.2 Sample Characterization

The model materials were investigated by scanning electron microscopy (SEM) and N_2 adsorption measurements. Furthermore, both, the bulk and the skeletal densities of the samples,

ρ and ρ_s, respectively, were determined after degassing at 110 °C for at least 20 h at pressures below 10^{-2} mbar. The skeleton densities of the samples were determined by He-pycnometry. The N_2 adsorption measurements were performed with a commercial volumetric sorption instrument (ASAP2010, Micromeritics). The resulting adsorption isotherms were evaluated for the combined specific micro- and mesopore volume $V_{Gurvich}$ [53] and the specific BET surface area S_{BET} [54], as well as the specific micropore volume V_{mic} and the specific external surface area S_{ext} by the t-plot method [55]. S_{ext} contains both, the macropore and mesopore surface area and can be roughly associated with the specific surface area of the mesopores, since the contribution of macropore surface area is here much smaller. The t-curve for the evaluation was calculated from the reference isotherm from ref [36], which was obtained on a similar sample exhibiting no micro- or mesoporosity. From the specific mesopore volume $V_{meso} = V_{Gurvich} - V_{mic}$ and the external surface area S_{ext}, the average mesopore diameter d_{meso} was estimated by $d_{meso} = 4V_{meso}/S_{ext}$. For further data evaluation we also calculated the mesoporosity of the struts within the sample $\phi_{meso} = V_{meso}/(V_{Gurvi} + 1/\rho_s)$ and the microporosity of the mesopore walls $\phi_{mic} = V_{mic}/(V_{mic} + 1/\rho_s)$.

The H_2O adsorption isotherms of all samples corresponding to the in-situ SANS and in-situ dilatometry experiments were measured by a commercial water vapor sorption instrument (SPS-11µ, prohumid). Prior to the H_2O adsorption measurements the samples were degassed at 50 °C for 24 h in a N_2 stream (purity 5.0).

2.3 In Situ Experiments

Small-angle neutron scattering (SANS) measurements were performed in-situ during Z-SLD water adsorption and desorption at 17 °C. They were performed at the SANS-1 instrument at the

Heinz Maier-Leibnitz Zentrum (MLZ) in Munich, Germany [56-57], utilizing a custom made in-situ sample cell designed for absolute vapor pressure control. The sample cell was connected to a custom made water vapor dosing manifold (including the water vapor source) and a pressure gauge. The *calcined* sample was measured in the same experimental session as the data presented previously [49]. The *as prepared* and the *sintered* samples were measured in a separate beamtime, where the sample cell was adapted in order to host both samples at the same time. Since sample equilibration is one of the main time-consuming steps, this made it possible to use the neutron beamtime efficiently while measuring a sufficient number of equilibrium points along the adsorption and desorption branches of the isotherms. The disadvantage of this setup was, however, that the in-situ dilatometry could not be measured simultaneously during the SANS experiments.

The measurement protocols used in the two experimental SANS sessions were very similar. Here we describe the one for the *as prepared* and the *sintered* samples, while the details for the *calcined* sample can be found elsewhere [49]. Prior to the SANS experiments the samples were heated to 50 °C, transferred to the sample cell in the hot state, and subsequently evacuated inside the sample cell for 2 h at a gas pressure smaller than 10^{-2} mbar. Then, the samples were cooled down to 17 °C using a thermostat connected to the sample cell body. During the SANS experiments the samples were subjected to pre-defined vapor pressure steps of Z-SLD water in a fully automated, iterative process. After an (unperturbed) equilibration time of 600 s for each relative water vapor pressure, SANS patterns and sample transmission were measured for 1500 s and 200 s, respectively. The neutron wavelength was λ = 0.55 nm, the collimation length was 6 m and the sample-detector distance was 5 m. The center of the 2D area detector was shifted with respect to the direct beam, allowing to cover an enlarged range of the scattering vector

length q ($q = 4\pi/\lambda \cdot sin\theta$ with 2θ being the scattering angle) in a single instrument configuration. The thickness of the finally prepared samples were 0.30 mm and 0.18 mm for the *as prepared* and the *sintered* samples, respectively, and 0.86 mm for the *calcined* sample. The reduced thickness of the *as prepared* and *sintered* samples ensured that in the given q-range multiple scattering could be neglected [58]. For the *calcined* sample a slight influence of multiple scattering was present and was corrected for in the data analysis [59].

The reduction of the SANS data was performed with the BERSANS software [60]. Background correction was performed by subtracting a transmission corrected empty cell measurement from the data. Corrected 2D SANS patterns were azimuthally averaged and scattering cross sections $d\Sigma/d\Omega\ (q)$ were obtained from absolute intensity calibration using the incoherent scattering of a pure H_2O sample of 1 mm thickness. The range of scattering vector lengths for the given instrument configuration was $0.15 \leq q \leq 2.2$ nm^{-1}. Since this q-range was too small to evaluate the incoherent scattering by using Porod's law as in Ref [49], we used another strategy to determine the incoherent scattering from H_2O. All three samples had been measured in their evacuated state with SANS covering an extended q-range at the same instrument in a previous session[49]. Therefore, the baselines for the incoherent scattering at $p/p_0 = 0$ could be determined using Porod's law. Then, the incoherent scattering was calculated for each pressure $p/p_0 > 0$ from the known water isotherms (Fig. 2b) using Eq. 1 from Ref [49]. After subtraction of the incoherent scattering of Z-SLD water, the reduced SANS profiles were evaluated with respect to the radial strain of the mesopore lattice by determining the relative shift of the first order Bragg reflection, leading to the *SANS strain isotherm* $\varepsilon_{SANS}(p/p_0)$. The detailed procedure to deduce the peak shift of the Bragg-peak has been described in Ref. [49].

The in-situ dilatometry measurements were performed simultaneously with the SANS measurement for the *calcined* sample, using a cell for combined SANS/dilatometry [49]. For the *as prepared* and *sintered* samples, dilatometry measurements were conducted using the mentioned in-situ dilatometric setup, with the same adsorbate under exactly the same conditions in the home laboratory several days before the in-situ SANS experiments. Prior to the dilatometry measurements, the samples were degassed in the same way as for the in-situ SANS runs, i.e., at a temperature of 50 °C for 2 h at pressures below 10^{-2} mbar. The result of the in-situ dilatometry measurement is the *dilatometric strain isotherm* $\varepsilon_{dil}(p/p_0)$, i.e., the relative length change ε_{dil} of the monolithic sample as a function of the relative pressure p/p_0.

3. Results and Discussion

3.1 Sample Characterization

The monolithic silica samples with a typical cylindrical shape (about 5 mm diameter and several cm length) exhibit a hierarchical porosity with macro-, meso, and micropores. Scanning electron microscopy (SEM) images of the *as prepared* sample are shown in **Fig. 1 a,b**. The SEM images of the other samples are very similar and are not shown here. The SEM images reveal that the samples consist of a disordered 3-dimensional network of cylindrical struts, which comprise ordered cylindrical mesopores with a pore distance of roughly 10 nm. The N_2 adsorption isotherms are presented in **Fig. 2a,** and the resulting structural parameters deduced from these isotherms are given in **Table 1** along with the results of the density measurements.

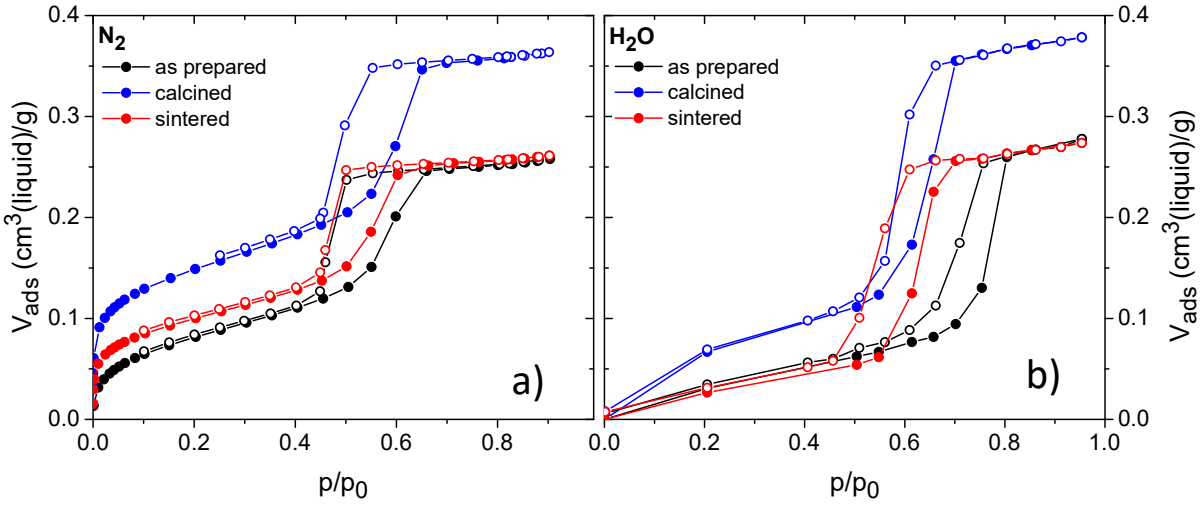

Figure 2: *N_2 (a) and H_2O (b) adsorption isotherms in units of specific liquid volume for all three samples. Full symbols denote adsorption, open symbols denote desorption.*

The mesopore structure from SEM is supported by the N_2 adsorption isotherms, which are of type IV(a) (IUPAC classification [61]) characteristic for mesoporous materials, and also by the SANS patterns (**Fig. 3**), featuring the hexagonal pore lattice arrangement. In the following, the different samples are compared with respect to their structural characteristics, and the impact of calcination and sintering is discussed.

Table 1: *Densities and pore space characteristics derived from N_2 adsorption: macroscopic density ρ, density of the nonporous skeleton ρ_s, specific pore volume $V_{Gurvich}$, specific micropore volume V_{mic}, specific mesopore volume V_{meso}, specific external surface area S_{ext}, average mesopore diameter d_{meso} as well as mesoporosity ϕ_{meso} and microporosity ϕ_{micro} of the struts within the sample.*

sample	ρ [g/cm³]	ρ_s [g/cm³]	$V_{Gurvich}$ [cm³/g]	V_{mic} [cm³/g]	V_{meso} [cm³/g]	S_{ext} [m²/g]	d_{meso} [nm]	ϕ_{meso}	ϕ_{micro}
as prepared	0.421	1.74	0.258	0	0.258	211	4.9	0.31	-
calcined	0.372	2.21	0.364	0.05	0.314	243	5.2	0.38	0.10
sintered	0.465	2.21	0.261	0.02	0.241	197	4.9	0.34	0.04

First, the *as prepared* and *calcined* samples are considered. For the *as prepared* sample the skeleton density ρ_s = 1.74 g/cm³ is significantly lower than the density of amorphous silica found in literature (ρ_s = 2.1 ± 0.1 cm³/g) [62]. The reason for this rather low density is the presence of organic residues within the skeleton. The calcination step removes the organic residues and ρ_s becomes comparable to amorphous silica (**Table 1**). The weight loss upon calcination corresponds to an organic content of approximately 25 wt% in the *as prepared* sample. Contrary to ρ_s, the bulk density ρ is significantly reduced by the calcination due to the removal of the organic phase. Noteworthy, the decrease of ρ by calcination is below 25 %, indicating shrinkage of the monolith disks in parallel to the mass loss.

The evaluation of the N_2 adsorption isotherms reveals that calcination results in an increase of the specific external surface area and specific mesopore volume as well as the average mesopore size. However, all these changes are on the order of 10 %. Furthermore, calcination induces microporosity into the sample, which was not present in the *as prepared* sample. We presume that the micropores already exist in the *as prepared* sample but are not accessible for gas adsorption due to their occupation by the organic residues.

Comparing *calcined* and *sintered* samples, it becomes evident that the sintering step induces shrinkage of material on all length scales: the bulk density of the monolithic samples increases, while the average mesopore diameter and the specific mesopore volume decrease. Furthermore,

the sintering process significantly reduces the specific micropore volume of the material, which was the primary goal of this post treatment.

The water adsorption isotherms of all samples presented in **Fig. 2b** are generally in line with the results obtained from N_2 adsorption. The H_2O adsorption isotherm of the *calcined* sample exhibits higher H_2O uptake when compared to the other two samples due to micropore filling and increased specific mesopore volume. Noteworthy, the overall uptake in terms of liquid filled pores is essentially the same for N_2 and H_2O for all samples, i.e., both adsorbates can be expected to access the same pore structures. An obvious discrepancy between N_2 and H_2O adsorption data is found with respect to the position of the hysteresis loop of the *as prepared* sample. For N_2 adsorption the hysteresis loops of all samples are located approximately in the same relative pressure range, while for H_2O adsorption the hysteresis loop of the *as prepared* sample is found at considerably higher relative pressure than for the other two samples. As the hysteresis position is a function of pore size and contact angle between liquid and solid phase, this indicates that the surface of the *as prepared* sample exhibits a higher hydrophobicity or different loading mechanism than amorphous silica due to the organic residues within the mesopore walls (compare ref [63]).

3.2 In-situ Experiments

The adsorbate used for the in-situ SANS experiment was a mixture of 91.95 wt% water (H_2O) and 8.05 wt% heavy water (D_2O) leading to a zero coherent neutron scattering length density (Z-SLD). Hence, no contrast changes are expected in the coherent scattering due to the adsorption of Z-SLD water within the samples. Therefore, the strain isotherms evaluated from in-situ

scattering data can be considered free of artifacts from contrast changes between different levels of pore filling, which are known to bear problems when using small-angle X-ray scattering (SAXS) for the determination of pore lattice deformation in such samples [46].

The reduced SANS profiles for the state of empty ($p/p_0 = 0$, solid lines) and filled ($p/p_0 = 0.95$, dashed lines) pores are shown for all samples in **Fig. 3a** in a double logarithmic representation. The overall shape of the SANS profiles is well in line with our previous study [49], although statistics at high q are not as good for the *as prepared* and the *sintered* samples due to the shorter measurement time and considerably thinner samples. **Fig. 3b** shows the SANS data in the q-region of the first order Bragg peak in a Kratky plot (scattering cross section multiplied by q^2 [44]). We observe two major effects: (i) a slight peak shift which is related to the mesopore lattice strain, and (ii) a reduction of peak intensity for the filled samples as compared to the empty samples. The relative drop of the integrated peak intensities are about 16 %, 3.6 % and ≈ 0.8 % for the *as prepared*, *calcined* and *sintered* samples, respectively. This finding is in line with our previous work [49], although an intensity change is at first sight not expected because adsorption of Z-SLD water in the pores does not change the contrast between pores and pore walls. Therefore, this intensity change must be either related to structural changes of the mesopore volume and/or the density of the mesopore walls, both being directly related to adsorption-induced deformation. A simple analytical model (Supplementary Information, chapter S1) reveals indeed that the observed intensity changes for the *sintered* and the *calcined* samples can be explained by a density change of the mesopore walls due to deformation of the micropores, which largely governs the measured strain ε_{SANS}. For the *as prepared* sample, however, the intensity drop of 16 % can by far not be explained simply by the volume change due to adsorption-induced deformation. Therefore, we must relate this intensity change at least partially to the organic

residues present in the sample. In fact, we expect these - presumably hydrophobic, see the shifted capillary condensation regime in **Fig. 2b** - organic residues to partly decorate the mesopore walls. Increasing water uptake in the samples could lead to a conformational change of these residues, which would naturally lead to an intensity change in the SANS data. Whether this results in an intensity increase or decrease will strongly depend on the type of conformation change, and the distribution of the organic material in the sample. Moreover, also an influence of preferential adsorption[64-65] or absorption[66] of D_2O on the measured intensity changes cannot be fully excluded. Since we do not have any reliable information on this, we abstain from making any further quantification attempts here. Nevertheless, the integrated intensity for the sintered sample being free of organics and containing almost no micropores proves that Z-SLD was correctly adjusted.

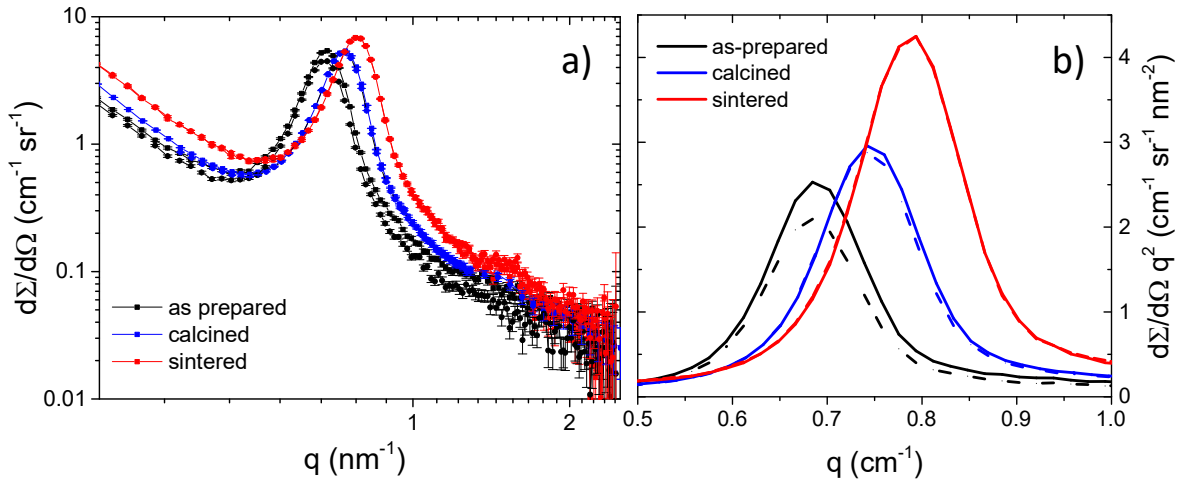

Figure 3: *SANS differential scattering cross section versus scattering vector length q for the as prepared (black), calcined (blue) and sintered (red) samples in vacuum ($p/p_0 = 0$, solid lines) and at a relative pressure of $p/p_0 = 0.95$ (dashed lines). (a) shows a double-logarithmic plot of*

the SANS data after subtraction of the incoherent scattering, while (b) shows a detail of the first order Bragg peaks in a Kratky-plot representation.

The SANS strain isotherms obtained from the relative shift of the Bragg peaks with respect to the reference state at $p/p_0 = 0$ are shown in **Fig. 4a,** showing a typical shape associated with mesoporous solids [13, 43]. They exhibit a hysteresis with the strain in the filled pore state being lower than in the film state in the pressure region close to capillary condensation/evaporation. The strain isotherms from in-situ dilatometry are shown in **Fig. 4b**. They are close to the results from SANS, except for a less pronounced strain hysteresis in the region of capillary condensation. Notably, the SANS and dilatometry strains in the film state and close to saturation pressure are almost identical. In this regard, the data presented in **Fig. 4** clearly differ from our previous comparison of in-situ dilatometry and in-situ small angle X-ray scattering [43]. This discrepancy can be explained by the already mentioned "apparent strains" originating from subtle contrast effects when using SAXS [46], while in the case of SANS with Z-SLD water this effect is explicitly excluded.

The largest net strain is found close to saturation pressure for all three samples. This strain is roughly 0.65 % for the *as prepared* sample, while the *calcined* sample exhibits about a factor of two, and the *sintered* sample nearly an order of magnitude smaller strain. This is in qualitative agreement with the results from N_2 adsorption in a similar series of samples in ref [37], although the absolute values of the strains appear to be higher for water adsorption. For further discussion it is important to keep in mind that the strain evaluated from SANS is due to deformation of the mesopore lattice, corresponding to the radial strain of the single struts, while dilatometry determines the strain of the macroporous strut network. Consequently, the strains obtained from the two techniques may be different [36-37], as will be discussed in the next section.

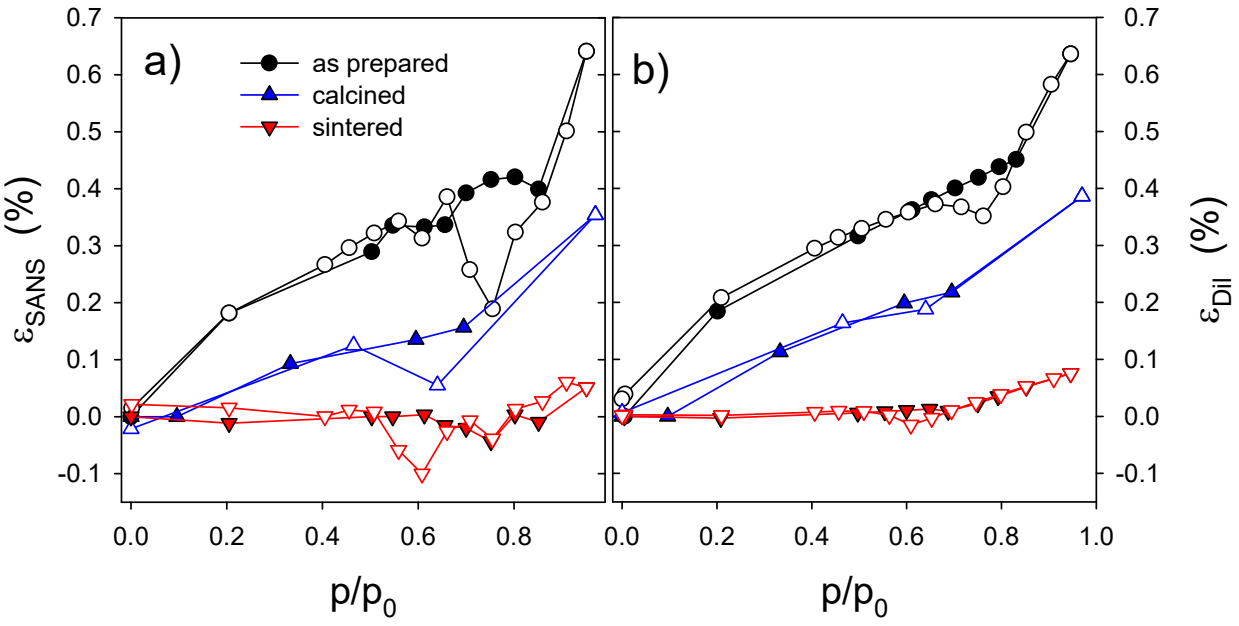

Figure 4: *Strain isotherms obtained from SANS (ε_{SANS}) and from dilatometry (ε_{Dil}) for the adsorption of Z-SLD water at 17 °C for the as prepared (black), calcined (blue) and sintered (red) samples. Full symbols denote adsorption, open symbols denote desorption. Lines between the measured points are included as guide to the eye. Scattering of the strain data derived from SANS are due to limited resolution.*

3.3 Modeling of the strain isotherms with the adsorption-stress model

For the quantitative description of the experimental strain isotherms obtained from in-situ dilatometry and in-situ SANS, we apply the theoretical framework presented in detail in refs [36-37]. A major challenge for this approach in the present work are the unknown adsorption properties of the silica surface for water at 17 °C, which are very sensitive to the amount and quality of the surface groups still present after the sintering process. To work around this problem, we utilized the structural information obtained from N_2 adsorption. We applied DBdB

theory for a cylindrical mesopore to calculate the specific adsorbed volume V_{ads} of N_2 for the film- and the filled case

$$V_{ads,film}\left(\frac{p}{p_0}\right) = S \cdot \left(h\left(\frac{p}{p_0}\right) - \frac{h\left(\frac{p}{p_0}\right)^2}{2R} \right) \quad \text{and} \quad V_{ads,filled}\left(\frac{p}{p_0}\right) = \frac{1}{2} \cdot S \cdot R \qquad (1)$$

where S is the specific mesopore surface (and R is the mesopore radius. The film thickness h is determined from the disjoining pressure by using the condition of thermodynamic equilibrium (Supplementary Information, **Eq. S3**). The disjoining pressure isotherm $\Pi(h)$ was obtained from the fit of a N_2 reference isotherm from a purely macroporous silica sample [36], using four fitting parameters, Π_1, Π_2, λ_1, λ_2 [42]

$$\Pi(h) = \Pi_1 e^{-h/\lambda_1} + \Pi_2 e^{-h/\lambda_2} \quad (2).$$

Micropore adsorption was taken into account by considering superposition of **Eq. 1** with a simple Langmuir isotherm

$$V_{ads,mic}\left(\frac{p}{p_0}\right) = V_{mic} \cdot \frac{b \cdot \frac{p}{p_0}}{1 + b \cdot \frac{p}{p_0}} \quad (3)$$

with an N_2–micropore interaction parameter b chosen to properly describe the low-pressure regime of the N_2 isotherm. The structural parameters $R = d_{meso}/2$, $S = S_{ext}$ and V_{mic} were taken from **Table 1**. This procedure gives a reasonable description of the N_2 adsorption isotherms from the *sintered* and the *calcined* samples, respectively, except for the detailed shape and width of the hysteresis (see **Figs. S1** and **S2**, SI). We note that the parameter b (**Table 2**) is considerably smaller than compared to the values found for samples with similar thermal history in ref [37], and also the hysteresis part of the present sample is less well described by the DBdB theory using the same reference isotherm. We attribute these differences to the aging of the present sample series at 50 °C / 74% humidity for several weeks, as this procedure may have

significantly changed the micropore size distribution and possibly also the interaction of the micro- and mesopores with N_2.

For the modeling of the corresponding water adsorption isotherms, we now take advantage of the fact that N_2 and H_2O access the same pore volume (see **Fig. 2**), and thus the structural parameters d_{meso}, S_{ext} and V_{mic} can be considered as given. This allowed for adapting the parameters of the H_2O disjoining pressure (**Eq. 2**), resulting in an approximate description of the H_2O adsorption isotherms. **Figs. 5a** and **6a** demonstrate that this procedure leads to a satisfactory representation of the water adsorption isotherms of the *calcined* and the *sintered* samples, respectively, although there are some deviations in particular concerning the width of the hysteresis. The adapted parameters for the calculation of the disjoining pressure isotherms are given in **Table S1**, SI, and the values for b are listed in **Table 2**.

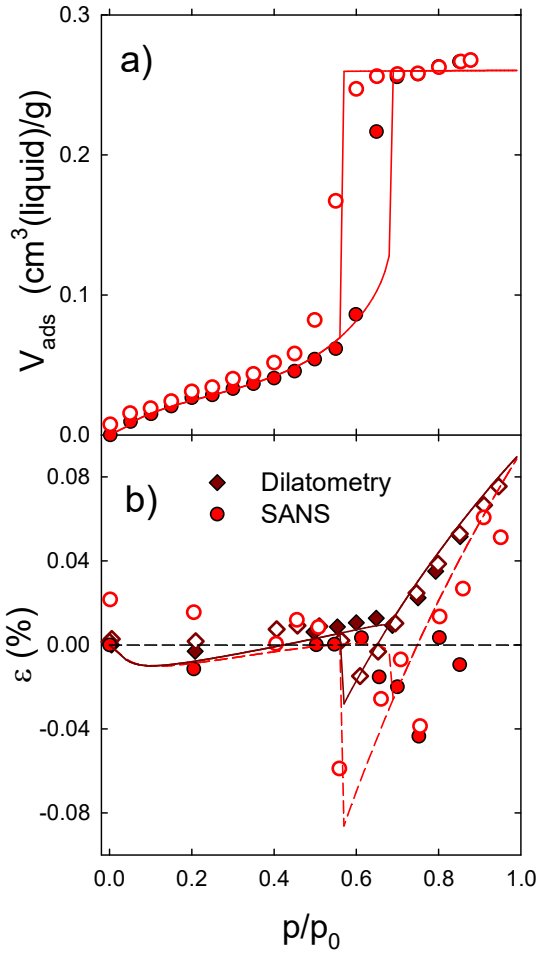

Figure 5: *a) H_2O adsorption isotherm (17 °C) of the sintered sample (closed symbols: adsorption, open symbols: desorption) modeled using the structural parameters from N_2 adsorption given in Table 1 and properly adapted parameters for the disjoining pressure. b) H_2O strain isotherms from SANS (red circles) and dilatometry (dark red diamonds). The lines result from the modeling of the SANS data (dashed line) and dilatometry data (solid line).*

Based on the modeling of the H_2O adsorption isotherm, we now applied the theoretical approach for the modeling of the axial and radial strain isotherms for cylindrical mesopores [36], and considered additionally the strain due to micropore deformation by applying the model outlined in ref [37], with all relevant equations being summarized in the SI. It needs to be noted that

the axial (σ_a) and radial (σ_r) stresses in the mesopores are uniquely determined by the modeling of the adsorption isotherms (**Eqs. S7-S10**, SI), and that the stress σ_{mic} within the micropores given by (**Eq. S14**, SI)

$$\sigma_{mic} = \frac{R_g T}{V_L}\left[\ln\left(b \cdot \frac{p}{p_0} + 1\right) + \frac{\partial b}{\partial \varepsilon_{mic}} \cdot \frac{\frac{p}{p_0}}{b \cdot \frac{p}{p_0} + 1}\right] \quad (4)$$

contains only one adjustable parameter $\partial b/\partial \varepsilon_{mic}$, which describes the variation of the adsorbate-micropore interaction b with the micropore strain according to the Shuttleworth relation [67]. From these stresses, the total linear strain in the radial mesopore direction is given by [37]

$$\varepsilon_{SANS} = \frac{1}{3}\varepsilon_{mic} + \varepsilon_{r,meso}$$

$$= \frac{1}{E}\left(\phi_{mic}(1-2\nu)\sigma_{mic} + \frac{\phi_{meso}}{1-\phi_{meso}}(2\sigma_r - \nu\sigma_a)\right) \quad (5).$$

Taking the micro- and mesoporosity from **Table 1**, there are only two adjustable parameters when modeling the SANS strain isotherm, namely the Young's modulus E of the mesopore walls (after fixing the Poisson ratio to $\nu = 0.2$ [36-37]) and $\partial b/\partial \varepsilon_{mic}$ from **Eq. 4**. The resulting modeling of the SANS strain isotherm for the *sintered* sample is shown in **Fig. 5b** (red dashed line). The parameter $\partial b/\partial \varepsilon_{mic}$ determines strongly the slope of the strain isotherms in the film regime and also predicts correctly the slightly negative strain at low pressures for this sample. The Young's modulus of the mesopore walls for the *sintered* sample is $E = 40\ GPa$, which is very close to the value of $E = 42\ GPa$ obtained from the N_2 strain isotherm of a sample with similar thermal history but different drying process [37].

After successful modeling of the SANS strain isotherm, the macroscopic strain obtained from dilatometry can be determined from the volumetric micropore strain ε_{mic} and a linear combination of axial and radial mesopore strains,

$$\varepsilon_{Dil} = \frac{1}{3}\varepsilon_{mic} + x\varepsilon_{r,meso} + (1-x)\varepsilon_{a,meso}$$

$$= \frac{1}{E}\left(\phi_{mic}(1-2\nu)\sigma_{mic} + \frac{\phi_{meso}}{1-\phi_{meso}}\{x(2\sigma_{\mathrm{r}} - \nu\sigma_a) + (1-x)(\sigma_a - 2\nu\sigma_{\mathrm{r}})\}\right) \quad (6)\,,$$

where the parameter x (see **Fig. 1**) was introduced in ref [36] to describe the relative contributions of axial and radial strains to the deformation of the macroscopic network. The modeling result of the dilatometric strain for the *sintered* sample with x as the only free parameter is shown in **Fig. 5b** (dark red line). The agreement with the experimental data is excellent, but the obtained value of $x = 0.5$ is different from the one found in the previous papers ($x = 0.33$), where dilatometric strain isotherms from N_2 adsorption were evaluated [36-37]. Possible reasons for this discrepancy will be discussed further below. Noteworthy, the calculated strain isotherms show a non-monotonic behavior at low pressures that could be explained by the contraction due to water adsorption of residual micropores still present after sintering. This effect is small, yet it is comparable with dilatometry experiments on microporous carbon monoliths [68].

We also note that water adsorption on the *sintered* sample leads to an almost flat strain isotherm in the film regime, which is quite different from the corresponding N_2 strain isotherm of a similar sample (compare **Fig. 5b** with **Fig. S1** in [37]). To get a better understanding of the impact of micropores on the water strain isotherms, we consider now the *calcined* sample in the next step. First, we note that the parameters describing the disjoining pressure isotherm for the *calcined* sample are different from the *sintered* sample (see **Table S1)**. This is in contrast to the N_2 adsorption isotherms of these two samples, which could both be described by the same disjoining pressure isotherm. The modeling of the SANS strain isotherm using E and $\partial b/\partial\varepsilon_{mic}$

as adjustable parameters yields again satisfactory agreement with the measured data (**Fig. 6b**). The Young's modulus of the wall for the *calcined* sample is $E = 20\ GPa$, which is again in fair agreement with the result from N_2 adsorption from a sample with similar thermal history ($E = 27\ GPa$ [37]). This underlines that within certain limitations to be discussed below, the theoretical framework outlined in [36-37] is capable of giving a reasonable description of both, the SANS and the dilatometric strain isotherms during water adsorption, and to reliably estimate the Young's moduli of the mesopore walls from these data.

However, the parameter $x = 0.65$ obtained from the modeling of the dilatometric strain isotherm of the *calcined* sample deviates even more from the value of 0.33 expected from the earlier work with N_2 adsorption [36-37]. We recall that the modeling of the adsorption isotherm in the first step determines all parameters of the model except the parameters $\partial b/\partial \varepsilon_{mic}$ (**Eq. 4**), as well as *x* and *E* **(Eq. 6)**, with *E* being just a simple multiplicative parameter for the whole strain isotherm. We also note that the dilatometry strain isotherms are statistically more reliable due to the inherently better strain resolution of dilatometry as compared to SANS. Therefore, we tried alternatively to fix *x* to the value of 0.33 and model the dilatometry data, leaving *E* and $\partial b/\partial \varepsilon_{mic}$ as free parameters. However, taking the modeling of the adsorption isotherms as given, it was not possible to get a physically meaningful agreement of the dilatometry data with **Eq. 6** given this restriction (see **Fig. S3**, SI).

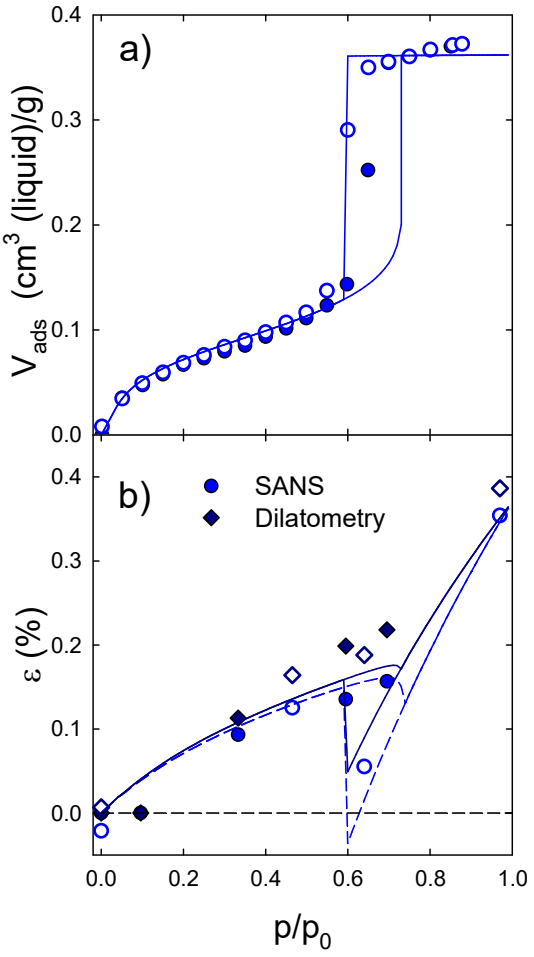

Figure 6: *a) H_2O adsorption isotherm (17 °C) of the calcined sample (closed symbols: adsorption, open symbols: desorption) modeled using the structural parameters from N_2 adsorption given in Table 1 and properly adapted parameters for the disjoining pressure. b) H_2O strain isotherms from SANS (blue circles) and dilatometry (dark blue diamonds). The lines result from the modeling of the SANS data (dashed line) and dilatometry data (solid line).*

It is not easy to believe that the radial strain component should contribute equally (for the *sintered* sample) or even stronger (for the *calcined* sample) to the macroscopic strain as compared to the axial strain component. The macroporous network consists of cylindrical struts with an aspect ratio of at least 3:1 between strut lengths and strut diameter, with each strut

ending in two joints (see **Fig. 1**). This structure suggests a dominant influence of the axial strain in the single struts to the macroscopic strain, as long as the joints are sufficiently rigid. Indeed, all dilatometry strain data on N_2 adsorption from the previous sample set could be well described by assuming $x = 0.33$ [37].

We can certainly not exclude a different deformation behavior of the macroporous network of the samples in the present work, since the adsorbate is water and the resulting strains are considerably higher as compared to N_2 adsorption. Also the mechanical properties of the connecting joints might have changed due to the aging process of the samples in order to get them stable for water adsorption. Moreover, the theoretical model does not take anisotropy of the elastic properties of the mesopore walls into account, which could be a consequence of directional, non-spherical micropores [69-71]. Yet, also another qualitative explanation for the observed discrepancy may be reasonable as follows:

The theoretical model for anisotropic deformation of cylindrical mesopores predicts the major differences between the axial and the radial strains in the hysteresis region of capillary condensation/evaporation, while for the film region the two strain components should be very similar, and for the completely filled pores they should be identical [36]. Therefore, the determination of the parameter x will particularly depend on the quality of the modeling in the capillary condensation/evaporation regime. It is seen already in the N_2 isotherms of the *sintered* and *calcined* samples (see **Figs. S1** and **S2**) that the adsorption isotherm modeling is not as good as compared to the samples used in [37]. In particular, the condensation/evaporation branches are strongly tilted. Also the water isotherms are not so well described in this regime (**Figs. 5a** and **6a**). Thus, we might attribute the discrepancy concerning the parameter x to an insufficient modeling of the adsorption isotherm, and hence also the strain isotherm, in the hysteresis region.

***Table 2**: Parameters used for modeling adsorption and strain isotherms for the sintered and the calcined samples. The Poisson ratio was fixed to $\nu = 0.2$ for all strain calculations.*

	Nitrogen isotherms *calcined* & *sintered*	water isotherms *sintered* sample	water isotherms *calcined* sample
b	500	20	30
$\partial b/\partial \varepsilon_{mic}$	-	-70	-15
E [GPa]	-	40	20
x	-	0.5	0.65

Finally, we also discuss shortly the strain isotherm of the *as prepared* sample. Since the hysteresis of the water adsorption isotherm is strongly shifted with respect to the N_2 isotherm (see **Fig. 2**) no meaningful modeling of the strain isotherms was possible in this case. Yet, the overall shape of the strain isotherm is similar to the one of the *calcined* sample, although no micropores (or at least no accessible ones) are present in this sample. The considerably larger overall strain (see **Fig. 4**) at comparable mesopore structure (**Table 1**) suggests the wall modulus of this sample being clearly lower as compared to the *calcined* sample, which is in qualitative agreement with the data presented in [37]. We can assume that the organic residues in the mesopore walls lower the Young's modulus, since the skeletal density of this sample is lower than compared to the one of bulk silica. However, for this sample we also observed a much stronger intensity change than expected from the sole volume change due to adsorption induced deformation. Therefore, we surmise that there is a strongly different interaction of the water molecules with the organic residues as compared to silica, with even possible water *ab*sorption at

specific sites in the samples. Such a scenario is far from being covered by the model of pure *ad*sorption-induced deformation and will therefore not be discussed further.

4. Conclusion

It was shown that in-situ small-angle neutron scattering (SANS) using a zero scattering length density (Z-SLD) adsorbate is suitable to quantitatively measure adsorption-induced deformation of ordered meso-/microporous materials. This is a big advantage of neutrons as compared to X-rays, where contrast effects usually influence the measured strain isotherms [43, 45-46], making the quantitative modeling of the data difficult or even impossible. Moreover, if a Z-SLD fluid is adsorbed into a two-phase system (pores in silica), the changes of the integrated SANS intensity can be directly translates to mesopore volume changes and/or to density changes within the mesopore walls. It would therefore even be possible to obtain strain isotherms from samples with disordered porosity by quantitatively analyzing the integrated intensity changes during adsorption of a Z-SLD fluid[47].

It was demonstrated that even the adsorption of a complex polar fluid like water allows obtaining meaningful strain isotherms from silica samples with hierarchical porosity. These data could be analyzed quantitatively using theoretical models for adsorption-induced deformation, even though the details of the adsorbate-adsorbent interactions were not explicitly known. To this end, the data from nitrogen adsorption (where the interactions are known from a reference isotherm) and from water adsorption were combined to model the adsorption-induced deformation with only two adjustable parameters. Eventually, this permitted estimating mechanical properties of the materials directly at the level of the mesopore walls, which is to our knowledge not possible with other methods. In contrast to dilatometry, which requires monolithic macroscopic samples, the SANS strain isotherms may easily be obtained also from

powder samples like SBA-15 or MCM-41. Therefore, in-situ SANS opens a possibility to determine nanomechanical properties of a wide variety of ordered mesoporous materials which cannot be synthesized in monolithic form.

Associated content

Supporting information: SANS intensity change due to adsorption induced deformation by Z-SLD water; Theoretical modeling of adsorption isotherms and strain isotherms; Modeling of the N_2 adsorption isotherms and disjoining pressure parameters for H_2O

Acknowledgement

We acknowledge financial support from the Austrian Science Foundation FWF (Project I 1605-N20), the German Science Foundation DFG (Project GZ: RE1148/10-1), and the US National Science Foundation (award No 1834339 to AVN). This work is based upon experiments performed at the SANS-1 instrument operated by HZG and FRM II at the Heinz Maier-Leibnitz Zentrum (MLZ), Garching, Germany.

References

1. Gor, G. Y.; Huber, P.; Bernstein, N., Adsorption-induced deformation of nanoporous materials-A review. *Applied Physics Reviews* **2017,** *4* (1), 011303.
2. Scherer, G. W.; Smith, D. M.; Stein, D., Deformation of Aerogels during Characterization. *Journal of Non-Crystalline Solids* **1995,** *186*, 309-315.
3. Reichenauer, G.; Scherer, G. W., Nitrogen adsorption in compliant materials. *Journal of Non-Crystalline Solids* **2000,** *277* (2-3), 162-172.
4. Champeau, M.; Thomassin, J. M.; Jerome, C.; Tassaing, T., In situ FTIR micro-spectroscopy to investigate polymeric fibers under supercritical carbon dioxide: CO2 sorption and swelling measurements. *Journal of Supercritical Fluids* **2014,** *90*, 44-52.
5. Biener, J.; Wittstock, A.; Zepeda-Ruiz, L. A.; Biener, M. M.; Zielasek, V.; Kramer, D.; Viswanath, R. N.; Weissmuller, J.; Baumer, M.; Hamza, A. V., Surface-chemistry-driven actuation in nanoporous gold. *Nature Materials* **2009,** *8* (1), 47-51.

6. Boudot, M.; Elettro, H.; Grosso, D., Converting Water Adsorption and Capillary Condensation in Usable Forces with Simple Porous Inorganic Thin Films. *ACS Nano* **2016,** *10* (11), 10031-10040.
7. Okada, K.; Asakura, G.; Yamamoto, T.; Tokudome, Y.; Takahashi, M., Anisotropic and Reversible Deformation of Mesopores and Mesostructures in Silica-Based Films under Mechanical Stimuli toward Adaptive Optical Components. *ACS Applied Nano Materials* **2019,** *2* (4), 2377-2382.
8. Bangham, D. H.; Fakhoury, N., The expansion of charcoal accompanying sorption of gases and vapours. *Nature* **1928,** *122*, 681-682.
9. Scherer, G. W., Dilatation of Porous-Glass. *Journal of the American Ceramic Society* **1986,** *69* (6), 473-480.
10. Dolino, G.; Bellet, D.; Faivre, C., Adsorption strains in porous silicon. *Physical Review B* **1996,** *54* (24), 17919-17929.
11. Mogilnikov, K. P.; Baklanov, M. R., Determination of Young's modulus of porous low-k films by ellipsometric porosimetry. *Electrochemical and Solid State Letters* **2002,** *5* (12), F29-F31.
12. Dourdain, S.; Britton, D. T.; Reichert, H.; Gibaud, A., Determination of the elastic modulus of mesoporous silica thin films by x-ray reflectivity via the capillary condensation of water. *Applied Physics Letters* **2008,** *93* (18).
13. Prass, J.; Mueter, D.; Fratzl, P.; Paris, O., Capillarity-driven deformation of ordered mesoporous silica. *Applied Physics Letters* **2009,** *95* (8), 083121.
14. Gor, G.; Bertinetti, L.; Bernstein, N.; Hofmann, T.; Fratzl, P.; Huber, P., Elastic response of mesoporous silicon to capillary pressures in the pores. *Applied Physics Letters* **2015,** *106*, 261901.
15. Grosman, A.; Puibasset, J.; Rolley, E., Adsorption-induced strain of a nanoscale silicon honeycomb. *EPL* **2015,** *109* (5), 56002.
16. Ustinov, E. A.; Do, D. D., Effect of adsorption deformation on thermodynamic characteristics of a fluid in slit pores at sub-critical conditions. *Carbon* **2006,** *44* (13), 2652-2663.
17. Ravikovitch, P. I.; Neimark, A. V., Density functional theory model of adsorption deformation. *Langmuir* **2006,** *22* (26), 10864-10868.
18. Kowalczyk, P.; Ciach, A.; Neimark, A. V., Adsorption-induced deformation of microporous carbons: Pore size distribution effect. *Langmuir* **2008,** *24* (13), 6603-6608.
19. Rouquerol, F. R., J.; Sing, K. S. W., *Adsorption by Powders and Porous Solids*. Academic Press: London, 1988.
20. Coussy, O., *Mechanics and Physics of Porous Solids*. Wiley: Hoboken, NJ, 2010.
21. Vandamme, M.; Brochard, L.; Lecampion, B.; Coussy, O., Adsorption and strain: The CO2-induced swelling of coal. *Journal of the Mechanics and Physics of Solids* **2010,** *58* (10), 1489-1505.
22. Pijaudier-Cabot, G.; Vermorel, R.; Miqueu, C.; Mendiboure, B., Revisiting poromechanics in the context of microporous materials. *Comptes Rendus Mecanique* **2011,** *339* (12), 770-778.
23. Vermorel, R.; Pijaudier-Cabot, G., Enhanced continuum poromechanics to account for adsorption induced swelling of saturated isotropic microporous materials. *European Journal of Mechanics a-Solids* **2014,** *44*, 148-156.
24. Neimark, A. V., Reconciliation of Gibbs Excess Adsorption Thermodynamics and Poromechanics of Nanoporous Materials In *Poromechanics VI: Proceedings of the Sixth Biot*

Conference on Poromechanics, Vandamme, M.; Dangla, P.; Pereira, J. M.; Ghabezloo, S., Eds. ASCE library: 2017; pp 56-63.
25. Perrier, L.; Pijaudier-Cabot, G.; Gregoire, D., Extended poromechanics for adsorption-induced swelling prediction in double porosity media: Modeling and experimental validation on activated carbon. *International Journal of Solids and Structures* **2018,** *146*, 192-202.
26. Shen, V. K.; Siderius, D. W.; Mahynski, N. A., Molecular simulation of capillary phase transitions in flexible porous materials. *Journal of Chemical Physics* **2018,** *148* (12), 124115.
27. Kolesnikov, A. L.; Georgi, N.; Budkov, Y. A.; Mollmer, J.; Hofmann, J.; Adolphs, J.; Glaser, R., Effects of Enhanced Flexibility and Pore Size Distribution on Adsorption-Induced Deformation of Mesoporous Materials. *Langmuir* **2018,** *34* (25), 7575-7584.
28. Zeng, Y. H.; Liu, L. M.; Zhang, H.; Do, D. D.; Nicholson, D., A Monte Carlo study of adsorption-induced deformation in wedge-shaped graphitic micropores. *Chemical Engineering Journal* **2018,** *346*, 672-681.
29. Gregoire, D.; Malheiro, C.; Miqueu, C., Estimation of adsorption-induced pore pressure and confinement in a nanoscopic slit pore by a density functional theory. *Continuum Mechanics and Thermodynamics* **2018,** *30* (2), 347-363.
30. Hlushak, S., Heat of adsorption, adsorption stress, and optimal storage of methane in slit and cylindrical carbon pores predicted by classical density functional theory. *Physical Chemistry Chemical Physics* **2018,** *20* (2), 872-888.
31. Vandamme, M., Coupling between adsorption and mechanics (and vice versa). *Current Opinion in Chemical Engineering* **2019,** *24*, 12-18.
32. Zhou, T. T.; Ioannidou, K.; Masoero, E.; Mirzadeh, M.; Pellenq, R. J. M.; Bazant, M. Z., Capillary Stress and Structural Relaxation in Moist Granular Materials. *Langmuir* **2019,** *35* (12), 4397-4402.
33. Derjaguin, B., A theory of capillary condensation in the pores of sorbents and of other capillary phenomena taking into account the disjoining action of polymolecular liquid films. *Acta Physicochimica Urss* **1940,** *12* (2), 181-200.
34. Broekhoff, J. C.; Deboer, J. H., Studies on Pore Systems in Catalysts .9. Calculation of Pore Distributions from Adsorption Branch of Nitrogen Sorption Isotherms in Case of Open Cylindrical Pores .A. Fundamental Equations. *Journal of Catalysis* **1967,** *9* (1), 8-14.
35. Broekhoff, J. C.; Deboer, J. H., Studies on Pore Systems in Catalysts .X. Calculations of Pore Distributions from Adsorption Branch of Nitrogen Sorption Isotherms in Case of Open Cylindrical Pores .B. Applications. *Journal of Catalysis* **1967,** *9* (1), 15-27.
36. Balzer, C.; Waag, A.; Gehret, S.; Reichenauer, G.; Putz, F.; Huesing, N.; Paris, O.; Bernstein, N.; Gor, G. Y.; Neimark, A. V., Adsorption-Induced Deformation of Hierarchically Structured Mesoporous Silica - Effect of Pore-Level Anisotropy. *Langmuir* **2017,** *33*, 5592-5602.
37. Balzer, C.; Waag, A. M.; Putz, F.; Huesing, N.; Paris, O.; Gor, G. Y.; Neimark, A. V.; Reichenauer, G., Mechanical Characterization of Hierarchical Structured Porous Silica by in Situ Dilatometry Measurements during Gas Adsorption *Langmuir* **2019,** *35*, 2948-2956.
38. Kresge, C. T.; Leonowicz, M. E.; Roth, W. J.; Vartuli, J. C.; Beck, J. S., Ordered mesoporous molecular-sieves synthesized by a liquid-crystal template mechanism. *Nature* **1992,** *359* (6397), 710-712.
39. Zhao, D. Y.; Feng, J. L.; Huo, Q. S.; Melosh, N.; Fredrickson, G. H.; Chmelka, B. F.; Stucky, G. D., Triblock copolymer syntheses of mesoporous silica with periodic 50 to 300 angstrom pores. *Science* **1998,** *279* (5350), 548-552.

40. Liu, M. C.; Wu, J.; Gan, Y. X.; Chen, C. Q., The pore-load modulus of ordered nanoporous materials with surface effects. *Aip Advances* **2016,** *6* (3).
41. Puibasset, J., Adsorption-Induced Deformation of a Nanoporous Material: Influence of the Fluid-Adsorbent Interaction and Surface Freezing on the Pore-Load Modulus Measurement. *Journal of Physical Chemistry C* **2017,** *121* (34), 18779-18788.
42. Gor, G. Y.; Paris, O.; Prass, J.; Russo, P. A.; Ribeiro Carrot, M. L.; Neimark, A. V., Adsorption of n-pentane on mesoporous silica and adsorbent deformation. *Langmuir* **2013,** *29*, 8601-8608.
43. Balzer, C.; Morak, R.; Erko, M.; Triantafillidis, C.; Husing, N.; Reichenauer, G.; Paris, O., Relationship Between Pore Structure and Sorption-Induced Deformation in Hierarchical Silica-Based Monoliths. *Zeitschrift für Physikalische Chemie* **2015,** *229* (7-8), 1189–1209.
44. Glatter, O.; Kratky, O., *Small-angle X-ray scattering*. Academic Press: New York, 1983.
45. Albouy, P. A.; Ayral, A., Coupling X-ray scattering and nitrogen adsorption: An interesting approach for the characterization of ordered mesoporous materials. Application to hexagonal silica. *Chemistry of Materials* **2002,** *14* (8), 3391-3397.
46. Prass, J.; Muter, D.; Erko, M.; Paris, O., Apparent lattice expansion in ordered nanoporous silica during capillary condensation of fluids. *Journal of Applied Crystallography* **2012,** *45*, 798-806.
47. Reichenauer, G., Structural Characterization of Aerogels. . In *Aerogels Handbook*, Aegerter, M. A.; Leventis, N.; Koebel, M. M., Eds. Springer: New York, 2011; pp 449-498.
48. Bahadur, J.; Melnichenko, Y. B.; He, L.; Contescu, C. I.; Gallego, N. C.; Carmichael, J. R., SANS investigations of CO2 adsorption in microporous carbon. *Carbon* **2015,** *95*, 535-544.
49. Morak, R.; Braxmeier, S.; Ludescher, L.; Putz, F.; Busch, S.; Hüsing, N.; Reichenauer, G.; Paris, O., Quantifying adsorption induced deformation of nanoporous materials on different length scales. *Journal of Applied Crystallography* **2017,** *50*, 1404-1410.
50. Brandhuber, D.; Hüsing, N.; Raab, C. K.; Torma, V.; Peterlik, H., Cellular mesoscopically organized silica monoliths with tailored surface chemistry by one-step drying/extraction/surface modification processes. *Journal of Materials Chemistry* **2005,** *15* (18), 1801-1806.
51. Putz, F.; Morak, R.; Elsaesser, M. S.; Balzer, C.; Braxrneier, S.; Bernardi, J.; Paris, O.; Reichenauer, G.; Husing, N., Setting Directions: Anisotropy in Hierarchically Organized Porous Silica. *Chemistry of Materials* **2017,** *29* (18), 7969-7975.
52. Kleitz, F.; Schmidt, W.; Schuth, F., Calcination behavior of different surfactant-templated mesostructured silica materials. *Microporous and Mesoporous Materials* **2003,** *65* (1), 1-29.
53. Gurvich, L. G., Physio-Chemical Attractive Force. *J. Russ. Phys.-Chem. Soc.* **1915,** *47*, 805-827.
54. Brunauer, S.; Emmett, P. H.; Teller, E., Adsorption of gases in multimolecular layers. *Journal of the American Chemical Society* **1938,** *60*, 309-319.
55. Lippens, B. C.; de Boer, J. H., Studies on Pore Systems in Catalysts V. The t method. *J. Catal.* **1965,** *4* (3), 319–23.
56. Heinz Maier-Leibnitz Zentrum, SANS-1: Small angle neutron scattering. *Journal of large-scale research facilities JLSRF* **2015,** *1*, A10.
57. Muhlbauer, S.; Heinemann, A.; Wilhelm, A.; Karge, L.; Ostermann, A.; Defendi, I.; Schreyer, A.; Petry, W.; Gilles, R., The new small-angle neutron scattering instrument SANS-1

at MLZ-characterization and first results. *Nuclear Instruments & Methods in Physics Research Section a-Accelerators Spectrometers Detectors and Associated Equipment* **2016,** *832*, 297-305.
58. Grillo, I., Small-Angle Neutron Scattering and Applications in Soft Condensed Matter. In *Soft Matter Characterization*, Borsali, R.; Pecora, R., Eds. Springer: Dordrecht, Netherlands., 2008; pp 723–782.
59. Jensen, G. V.; Barker, J. G., Effects of multiple scattering encountered for various small-angle scattering model functions. *Journal of Applied Crystallography* **2018,** *51*, 1455-1466.
60. Keiderling, U., The new 'BerSANS-PC' software for reduction and treatment of small angle neutron scattering data. *Applied Physics a-Materials Science & Processing* **2002,** *74*, S1455-S1457.
61. Thommes, M.; Kaneko, K.; Neimark, A. V.; Olivier, J. P.; Rodriguez-Reinoso, F.; Rouquerol, J.; Sing, K. S. W., Physisorption of gases, with special reference to the evaluation of surface area and pore size distribution (IUPAC Technical Report). *Pure and Applied Chemistry* **2015,** *87* (9-10), 1051-1069.
62. Woignier, T.; Phalippou, J., Skeletal Density of Silica Aerogels. *Journal of Non-Crystalline Solids* **1987,** *93* (1), 17-21.
63. Gu, Z. Y.; Alexandridis, P., Sorption and transport of water vapor in amphiphilic block copolymer films. *Journal of Dispersion Science and Technology* **2004,** *25* (5), 619-629.
64. King, A.; James, F. W.; Lawson, C. G.; Briscoe, H. V. A., The selective adsorption of heavy water. *Journal of the Chemical Society* **1935**, 1545-1549.
65. Lin, Y.; Horita, J., An experimental study on isotope fractionation in a mesoporous silica-water system with implications for vadose-zone hydrology. *Geochimica Et Cosmochimica Acta* **2016,** *184*, 257-271.
66. Delajon, C.; Gutberlet, T.; Mohwald, H.; Krastev, R., Absorption of light and heavy water vapours in polyelectrolyte multilayer films. *Colloids and Surfaces B-Biointerfaces* **2009,** *74* (2), 462-467.
67. Shuttleworth, R., The surface tension of solids. *Proceedings of the Physical Society of London Section A* **1950,** *63* (365), 444-457.
68. Balzer, C.; Brameier, S.; Neimark, A. V.; Reichenauer, G., Deformation of Microporous Carbon during Adsorption of Nitrogen, Argon, Carbon Dioxide, and Water Studied by in Situ Dilatometry. *Langmuir* **2015,** *31* (45), 12512-12519.
69. Ryoo, R.; Ko, C. H.; Kruk, M.; Antochshuk, V.; Jaroniec, M., Block-copolymer-templated ordered mesoporous silica: Array of uniform mesopores or mesopore-micropore network? *Journal of Physical Chemistry B* **2000,** *104* (48), 11465-11471.
70. Solovyov, L. A.; Shmakov, A. N.; Zaikovskii, V. I.; Joo, S. H.; Ryoo, R., Detailed structure of the hexagonally packed mesostructured carbon material CMK-3. *Carbon* **2002,** *40* (13), 2477-2481.
71. Galarneau, A.; Cambon, N.; Di Renzo, F.; Ryoo, R.; Choi, M.; Fajula, F., Microporosity and connections between pores in SBA-15 mesostructured silicas as a function of the temperature of synthesis. *New Journal of Chemistry* **2003,** *27* (1), 73-79.

Table of Contents Graphic